Supplementary information: Topological Elasticity in Physical Gels with Limited Valence

Giorgia Palombo,[1] Simon Weir,[1] Davide Michieletto,[1,2,*] and Yair Augusto Gutiérrez Fosado[1,†]

[1] *School of Physics and Astronomy, University of Edinburgh, Peter Guthrie Tait Road, Edinburgh, EH9 3FD, UK*

[2] *MRC Human Genetics Unit, Institute of Genetics and Cancer, University of Edinburgh, Edinburgh EH4 2XU, UK*

I. NANOSTARS DESIGN

Nanostar motifs are assembled from three single-stranded (ss) oligonucleotides, 49 nucleotides long each and with sequences reported in Table S1. These motifs were designed using NUPACK [1], with minor modifications from those originally proposed in Ref. [2], and they consist of five functional parts. Each double-stranded (ds) DNA arm is 20 base-pairs (bp) long and is formed through the hybridization of segments I and II. The arms terminate in a self-complementary 6-nucleotide fragment with sequence 5'-CGATCG-3'. This sticky end is equal for all three arms, allowing the non-specific hybridization of two nanostars (ns): any of the three arms of one ns can hybridize with any (but only one) of the arms of another ns. Unpaired adenines (A) are introduced at the core of the Y-shaped structure and before the sticky end as flexible joints because they enhance the internal flexibility of the nanostar and the flexibility of the nanostar–nanostar bond, respectively.

Beyond structural features, the design provides certain stability. Using NUPACK and DINAmelt [3], we checked that at [NaCl]=150 mM and [ssDNA]=500 μM, the melting temperature of individual DNAns ($T_{m1} = 77^{\circ}C$) is larger than the melting temperature of the sticky-ends ($T_{m2} = 38^{\circ}C$). Therefore, for temperatures below T_{m2} and at concentrations $C > 300\mu M$, beyond the phase-separation region [4], we can form DNAns hydrogels.

Segment I	FJC	Segment II	FJ	Sticky end
5′– CTGGATCCGCGGAAGCTTAA	AA	CGGAATTCGCATGGATCCCC	A	CGATCG –3′
5′– GGGGATCCATGCGAATTCCG	AA	CTGAATTCCCTGGGATCCCG	A	CGATCG –3′
5′– CGGGATCCCAGGGAATTCAG	AA	TTAAGCTTCCGCGGATCCAG	A	CGATCG –3′

Table S1. Strand sequence used in the nanostar design with valence $f = 3$. Each row represents a different ssDNA oligonucleotide. Each oligonucleotide is 49 bases long and presents two segments (20 nucleotides long each) separated by two unpaired A-nucleotides entailing flexibility at the molecule's core (FJC). Segments with the same colour have complementary sequences to form the double-stranded arms. The sticky end of each oligonucleotide is preceded by an unpaired A-nucleotide forming a second flexible joint (FJ).

II. DETAILS OF SIMULATIONS

As described in the main text, we model DNA nanostars as rigid bodies made up of ten particles. Seven beads constitute the core of the molecule. Each bead has a diameter $\sigma \sim 2.5$ nm (or 8 bp) implemented via a truncated and shifted Lennard-Jones (LJ) potential:

$$U_{LJ}(r) = 4\epsilon \left[\left(\frac{\sigma}{r}\right)^{12} - \left(\frac{\sigma}{r}\right)^{6} + \frac{1}{4} \right], \qquad \text{(S1)}$$

if $r < 2^{1/6}\sigma$, and $U_{LJ}(r) = 0$ otherwise. Here $\epsilon = 1.0$ parameterises the strength of the repulsion, and r is the Euclidean distance between the beads.

Patches are placed at a distance of $2.5\sigma \sim 20$bp from the core of the molecule and on the surface of the outermost bead along each arm (see Fig. **1**(b) in the main text). To represent the sticky-ends interaction and to regulate the attraction between adjacent nanostars, we use a Morse potential:

$$U_m(r) = \epsilon_m \left[e^{-2\alpha_0(r-r_0)} - 2e^{-\alpha_0(r-r_0)} \right], \qquad \text{(S2)}$$

for $r < R_c$. Here, r represents the distance between patches of two nanostars, $r_0 = 0$ is their equilibrium distance, and $R_c = 0.2\sigma$ is the cut-off distance of attraction. We set $\epsilon_m = 25.0 k_B T$ and $\alpha_0 = 14\sigma^{-1}$ to control the amplitude and width of the potential, respectively. With these parameters the single-bond-per-patch condition holds in the bast majority of our results. At a given concentration, on average only 0.002%-0.025% of all the contacts in simulations with our model would not satisfy the one-to-one binding. Importantly, the hybridisation between DNAns is not permanent; there is a characteristic time (τ_c) for network reconfiguration in which nanostars unbind and bind again to a different ns.

The Langevin integration of the system was carried out using LAMMPS [5] in an NVT ensemble by a standard velocity-Verlet algorithm with integration time-step $dt = 0.01$. The position of particles in the system obeys the following equation:

$$m\frac{d^2\mathbf{r}}{dt^2} = -\mu\frac{d\mathbf{r}}{dt} - \nabla U + \sqrt{2k_B T\mu}\Lambda(t), \qquad \text{(S3)}$$

where U is the total potential field experience by a particle, $m = 1$ is the mass of the particle, $\mathbf{r}$ represents its

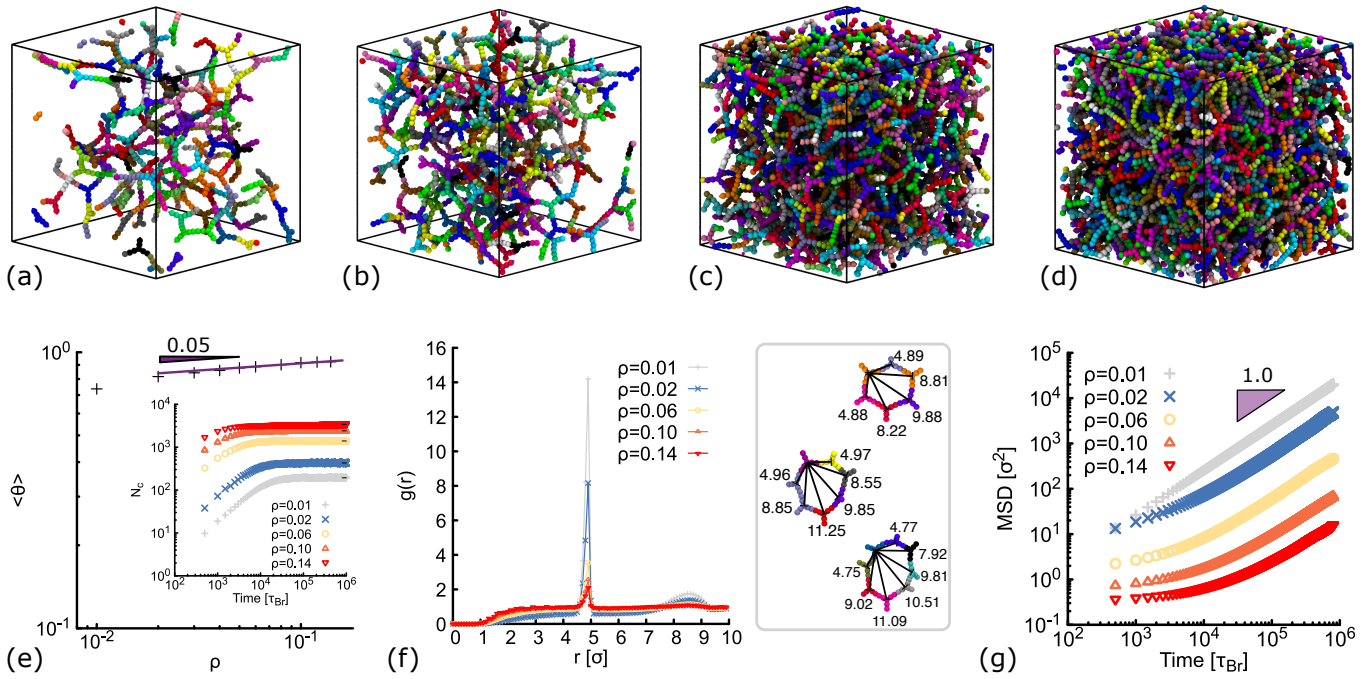

Figure S1. **Network assemble**. Panels **(a)-(d)** show snapshots of typical configurations from simulations after the network is formed, at the last time-step ($t = 10^6\tau_{Br}$) and at $\rho = 0.01, 0.02, 0.06$ and 0.1, respectively. **(e)** The curves in the inset represent the number of contacts N_c as function of time obtained during the network formation. The main plot shows the fraction of connected nanostars in the steady state as a function of the volume fraction. **(f)** In the left panel, the radial distribution function averaged over configurations at long times (when the network is formed) is shown. The right panel shows typical geometries found in simulations at $\rho = 0.01$. Black lines connect the core of two DNAns, and the labels show the distance (in simulation units) between them. **(g)** Log-log plots of the MSD averaged over all the molecules in the system.

position, μ is the friction and $\Lambda(t)$ is the white noise term with zero mean which satisfies $\langle\Lambda_\alpha(t)\Lambda_\beta(s)\rangle = \delta_{\alpha\beta}\delta(s-t)$ along each Cartesian coordinate represented by the Greek letters.

Equilibration and assemble of the network.

Initial configurations were produced by placing N nanostars in a cubic simulation box of length $L = 40\sigma$ and with periodic boundary conditions (PBC). The volume fraction of this system is $\rho = NV_1/L^3$, where $V_1 = 7\frac{4}{3}\pi(\sigma/2)^3$ is the excluded volume of one nanostar, given by the sum of the volume of all its structural beads. During equilibration, we turn-off the attraction between nanostars ($\epsilon_m = 0$) and integrate the system for $5 \times 10^5\tau_{Br}$. We then set the attraction between patches to $\epsilon_m = 25k_BT$, allowing in this way the network formation, and we run the system for $10^6\tau_{Br}$. Snapshots from simulations at the end of this run are depicted in Figs. S1(a)-(d) for different DNAns concentrations.

We compute the total number of contacts ($N_c(t)$) between DNAns at a fixed time-step by counting the number of pairs of patches that are at a distance $r \leq 0.2\sigma$. The temporal evolution of this quantity is reported in the inset of Fig. S1(e). At all concentrations, the system evolves to a steady state where the network is formed and $N_c(t)$ plateaus around an equilibrium value. The fraction of connected DNAns ($\langle\theta\rangle = 2N_c(t)/Nf$) in this steady state is obtained by averaging the value of N_c at $t \geq 2\times10^5\tau_{Br}$. The plot of $\langle\theta\rangle$ as a function of the volume fraction is reported in Fig. S1(e), from which we can extract the scaling $\langle\theta\rangle \sim \rho^{0.05}$, i.e. very weakly dependent on the volume fraction. Indeed, for most of the values of ρ explored in this work, the fraction of connected DNAns is always near unity.

Radial distribution function.

As an initial attempt to characterise the structure of our networks, we compute the radial distribution function (RDF), g(r), using only the position of beads at the core of the DNAns:

$$g(r) = \frac{1}{4\pi\phi M}\sum_{i=1}^{M}\sum_{j\neq i}^{M}\langle\delta(|r_{ij} - r|)\rangle, \qquad \text{(S4)}$$

where $\phi = N/L^3$ is the number density of core beads in the simulation, r_{ij} represents the distance between the

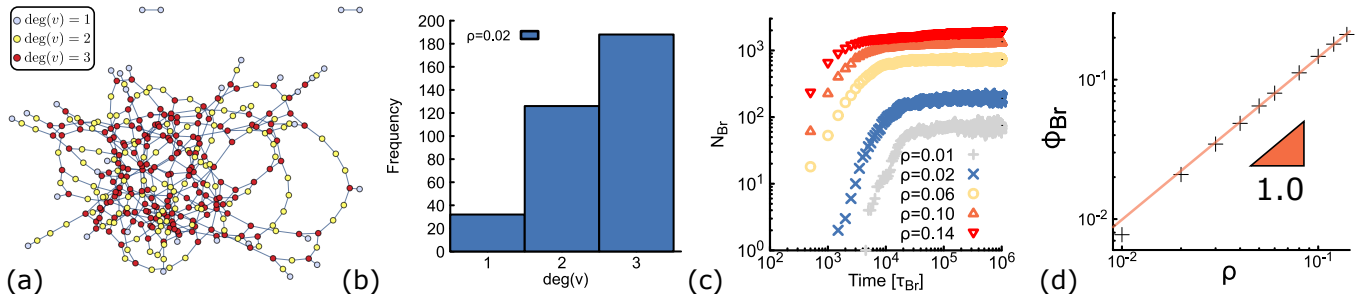

Figure S2. **Network diagram**. **(a)** Shows the network diagram corresponding to the system depicted in Fig. S1(b), at the last time-step ($t = 10^6\tau_{Br}$) of the simulation and at $\rho = 0.02$. **(b)** Histogram obtained from the network diagram in (a), depicting the frequency of each deg(v). **(c)** Curves represent the number of branching points (N_{br}) as a function of time obtained during the network formation. **(d)** Scaling of the fraction of branching points with the volume fraction.

cores of molecules i and j, and the sum counts the number of DNAns cores that are at a distance r. We compute $g(r)$ using the wrapped coordinates of nanostars in our simulations by: (i) Choosing the M core beads that are inside a sphere of radius $R_{select} = L/4$ with centre at the origin of the box. (ii) We loop over each of these M particles and count the number of core beads neighbours at a distance r. This search radius is always smaller or equal to $L/4$, and, in the count, we consider all the core beads in the simulation (not only the M selected in (i)). (iii) We replace this information in Eq. S4 to compute $g(r)$. Then, we repeat this procedure for all configurations from simulations in the steady state (at large times and when $\theta(t)$ has reached a plateau), and we take the average over configurations. Results at different concentrations are depicted in the left panel of Fig. S1(f). At all values of ρ, $g(r)$ displays a global maximum located close to $r = 5\sigma$. This corresponds to the average distance between the core of two bound nanostars. We note that at low concentrations, for instance at $\rho = 0.01$, a peak also appears at $7.5\sigma < r < 9\sigma$, with a local maximum at about $r = 8.5\sigma$, corresponding to the distance between second nearest neighbours. Loops made by nanostars observed in simulations are consistent with these results (see the right panel of Fig. S1(f)). As the nanostar concentration increases, the global maximum height decreases, and the second peak flattens, indicating a more heterogeneous, disordered network with broader distributions of structures and network loops.

Mean Squared Displacement

We compute the mean squared displacement of the centre of mass of nanostars after network formation using the relation:

$$\mathrm{MSD}(t) = \langle [\boldsymbol{r}_{CM}(t + t_0) - \boldsymbol{r}_{CM}(t_0)]^2 \rangle, \qquad \text{(S5)}$$

where the average is performed over nanostars and t_0. We report the MSD at different concentrations in Fig. S1(g). As expected, the system's mobility decreases as the nanostars concentration increases. We also note that while at $\rho = 0.01$, the MSD shows a diffusive behaviour, for larger values of ρ, the MSD displays a subdiffusive regime at early times, which ends in a freely diffusive regime at late times. This is a typical signature of viscoelastic behaviour that is also captured by the plateau of $G(t)$ in Fig. **1**(b) of the main text.

Network diagrams

A network diagram is a representation of the connection between nanostars at a given time-step in the simulation. We identify these connections by computing the distance between the $3 \times 3 = 9$ pair of patches belonging to two different nanostars. If any of the results is smaller than $R_c = 0.2\sigma$, the two nanostars involved are connected. This information is visually captured in a network diagram by drawing vertices representing nanostars and a line (also called edge) between any two connected nanostars. In Fig. S2(a), we show the network diagram for one of the snapshots from simulations at $\rho = 0.02$. Different colours represent the degree of a vertex (deg(v)), i.e., the number of DNA nanostars connected to that vertex. Since the valence of DNAns is $f = 3$, deg(v) can be either: 0 (for isolated stars, not shown in the plot), 1 (light-blue circles), 2 (yellow circles) or 3 (red circles). The histogram depicting the frequency of nanostars with a certain degree of connection is also shown in Fig. S2(b). As it can be seen, the number of branching points (fully connected DNAns, with deg(v) = 3) is larger than those of DNAns with deg(v) = 1 or 2. This is reflected in the higher density of red circles in the network diagram of Fig. S2(a). By repeating this process at different time-steps, we obtain the temporal evolution of the number of branching points ($N_{Br}(t)$) reported in Fig. S2(c). We observe that at all concentrations, $N_{Br}(t)$ reaches a plateau at long times, from which the number density of branching points

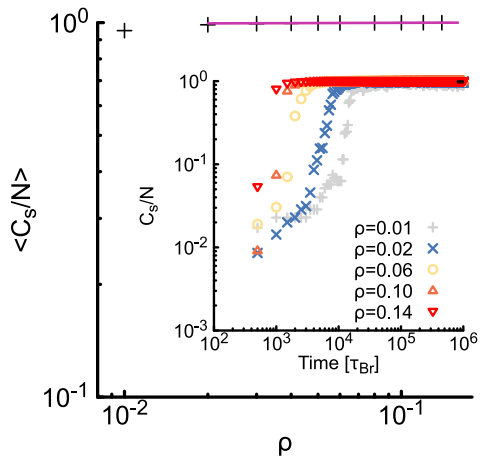

Figure S3. **Largest connected component**. Inset shows the time evolution of the number (C_s) of DNAns in the largest connected component, normalized by the number (N) of nanostars in the system. The main plot displays the scaling of C_s/N in the steady state with the concentration of DNAns.

($\phi_{Br} = N_{Br}/L^3$) is computed and reported in Fig. S2(d).

In network diagrams, a connected component is a set of vertices with edges spanning paths to connect any two of them. The larger the set of vertices in a component, the higher the degree of connectivity in the system. By inspecting the network diagram in Fig. S2(a), it is evident that most of the DNAns participate in the network, and a few of them form small clusters. Therefore, the degree of connectivity of the network is large. This can also be shown by computing the number (C_s) of DNAns that are part of the network's largest component. When $C_s = N$, only one cluster in the system is formed by the connection of all DNAns. In contrast, nanostars are split into clusters when the value of $C_s < N$. In the inset of Fig. S3, we show the time evolution of $C_s(t)/N$. We note that at all concentrations, the system reaches a plateau in which $C_s(t)/N \simeq 1$, indicating that nanostars are part of a single cluster spanning the size of the system. This is also reported in the main plot of Fig. S3, where we show that at the steady-state $C_s/N \simeq 1$ for $\rho \geq 0.02$. It is worth noting that the behaviour is markedly different in the case of soft colloidal gels (without limited valence). For instance, in Ref. [6] (section 9 of the supplementary information), the authors show that close to the gelation threshold, their network forms a percolating cluster with finite clusters separated from the backbone and therefore, C_s/N would be smaller than one. In our system, we form equilibrium gels and even liquids (see MSD of the system at lowest ρ) with a fully percolating cluster.

Shortest path between branching points

In graph theory, the shortest path from a source vertex to a target vertex is the path with the minimum number of edges between them. We use Mathematica [7] to find the shortest path connecting any two branching points in a network diagram. In Fig. S4(a), we give an example of this analysis for two branching points. As a result, we obtain the molecule IDs (labels) of the DNAns in the shortest path, which allows us to identify how this path looks in our simulations (see Left panel in Fig. S4(b)). Since we use periodic boundary conditions, an object which has passed through one face of the simulation box re-enters through the opposite face. Therefore, it is necessary to use the minimum image criterion (MIC) to reconstruct the shortest path (Right panel in Fig. S4(b)). For simplicity and computational efficiency, we reconstruct the shortest path and determine its radius of gyration ($R_{g,\lambda}$) by using only the core beads of nanostars:

$$R^2_{g,\lambda} = \frac{1}{\lambda}\sum_{n=1}^{\lambda}\left[\boldsymbol{r}_{\rm mean} - \boldsymbol{r}_n\right]^2, \tag{S6}$$

where $\boldsymbol{r}_n$, $\boldsymbol{r}_{\rm mean}$ and λ represent the position of the n-th core-bead of a DNAns in the shortest path, the centre of mass of the shortest path and its length, respectively. By repeating this process at different times after full network formation and at different concentrations, we obtain the distribution $P(\lambda)$ of the number of DNAns in the shortest path between branching points and the average of this distribution $\langle\lambda\rangle$ reported in Figs. S4(c)-(d), respectively. In the same way, we compute the average radius of gyration reported in Fig. S4(e). The scaling exponents obtained: $\langle R_{g,\lambda}\rangle \sim \rho^{0.06}$ and $\langle\lambda\rangle \sim \rho^{0.1}$, suggest that the shortest paths adopt conformations compatible to those of linear chains in a good solvent, $\langle R_{g,\lambda}\rangle \sim \langle\lambda\rangle^{0.6}$.

We also computed the average radius of gyration of the shortest path as a function of λ. Results for different concentrations are shown in Fig. S4(f). These results are compatible with the Flory exponent for self-avoiding walks, i.e., $\nu = 0.58$, and are also in line with our previous findings from the scaling of $\langle R_{g,\lambda}\rangle$ and $\langle\lambda\rangle$. The fractal dimension of the shortest paths is given by $d_f = 1/\nu = 1.7$. It is worth stressing here that the scaling reported in Fig. S4(f) appears to be independent of the concentration of nanostars, and so is d_f. This suggests that the network structure does not change its fractal dimension despite displaying different material behaviours (from liquid-like at $\rho = 0.01$ to gel-like at $\rho = 0.014$, see MSDs). This also suggests that there may be a different motif in the network that emerges when the gel changes its physical behaviour.

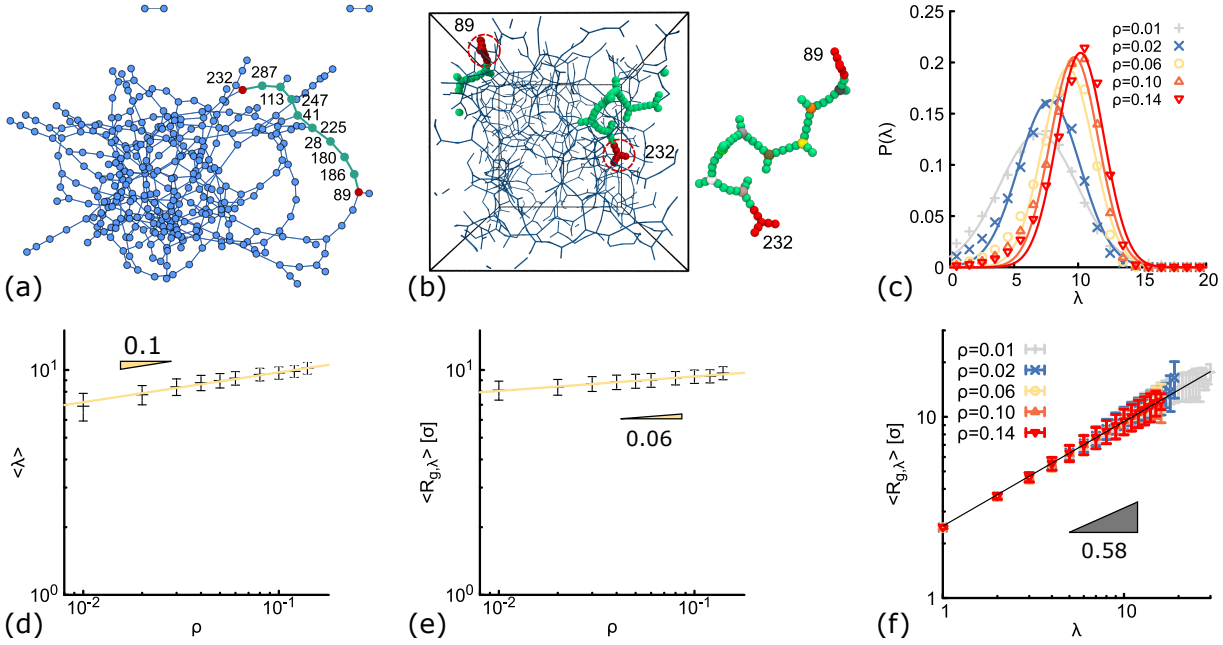

Figure S4. **The shortest path analysis**. **(a)** Shows the same network diagram as the one in Fig. S2(a), but with two branching points highlighted in red and the shortest path between them highlighted in green. Labels represent the molecule ID of nanostars. Note that the length of the shortest path is $\lambda = 9$ nanostars. **(b)** Left panel shows a snapshot from simulations corresponding to the network diagram in (a). Since the shortest path is formed through the periodic boundary conditions, we use the minimum image criterion to reconstruct the correct path (Right panel). To ease visualization, the core beads of nanostars are highlighted. **(c)** The probability distribution function of the shortest path. **(d)** Scaling of λ with the volume fraction of nanostars. **(e)** Scaling of the average radius of gyration of the shortest path as a function of ρ. **(f)** Plot of the radius of gyration (computed using Eq. S6) as function of the length λ, for different concentrations of nanostars.

Minimum loops

In the network diagrams, a loop is a closed path with no repetition of vertices or edges other than the starting and end points. Here, we compute all the loops ($N_{i,l}$) with size $l \in [4, l_m]$ nanostars, passing through the ith-vertex in a graph (note that $i \in [1, N]$). Since the number of loops $N_{i,l}$ increases exponentially with l_m, we restrict the search to only those loops formed by at the most $l_m = 20$ nanostars. The loop with the smallest size (created by the least number of DNAns, l_{min}) is the minimum loop passing through vertex i. We note that two or more vertices in the same graph could share a minimum loop; therefore, our algorithm ensures to exclude repeated minimum loops.

In Fig. S5(a) and (b), we show examples of this analysis for two different vertices in the same graph, $i = 247$ and $i = 150$, respectively. First, we obtain the molecule IDs of all nanostars in the minimum loops passing through those vertices using Mathematica graph analysis tools (corresponding snapshots from simulations are reported in panels (c) and (d)). We observe that in the former case, the minimum loop identified in the graph is actually a linear path (closed through the periodic boundary conditions and thus an artefact of the simulation setup), and that is formed by $l_{min} = 15$ nanostars. We avoid considering these paths by using: first, the minimum image criterion to reconstruct the minimum loops, and then, we impose the condition $R_{g,min} < 0.3L = 12\sigma$ on the radius of gyration of the minimum loop:

$$R^2_{g,min} = \frac{1}{l_{min}} \sum_{n=1}^{l_{min}} \left[\boldsymbol{r}_{\rm mean} - \boldsymbol{r}_n\right]^2 , \qquad \text{(S7)}$$

this time $\boldsymbol{r}_n$, $\boldsymbol{r}_{\rm mean}$ and l_{min} represent the position of the n-th core-bead of a DNAns in the minimum loop, its centre of mass and its size, respectively. Figure S5(d) shows a successfully identified minimum loop from our simulations, formed by $l_{min} = 9$ DNA nanostars.

By repeating this procedure for all the vertices in a graph (not only the branching points) and then for different time-steps, we obtain the temporal evolution of the total number of minimum loops ($N_{minloops}(t)$) that is reported in Fig. S5(e). At large times, $N_{minloops}(t)$ reaches a plateau for all concentrations, from which we produce the inset of Fig. **2**(f) in the main text, and we find the scaling $N_{minloops} \sim \rho$. We also obtain the distribution $P(l_{min})$ of the number of DNAns in the minimum loop depicted in Fig. **2**(e) of the main text, and the average of the distribution $\langle l_{min} \rangle$ (see Fig. **2**(f)). Likewise, here we obtain the average radius of gyration in

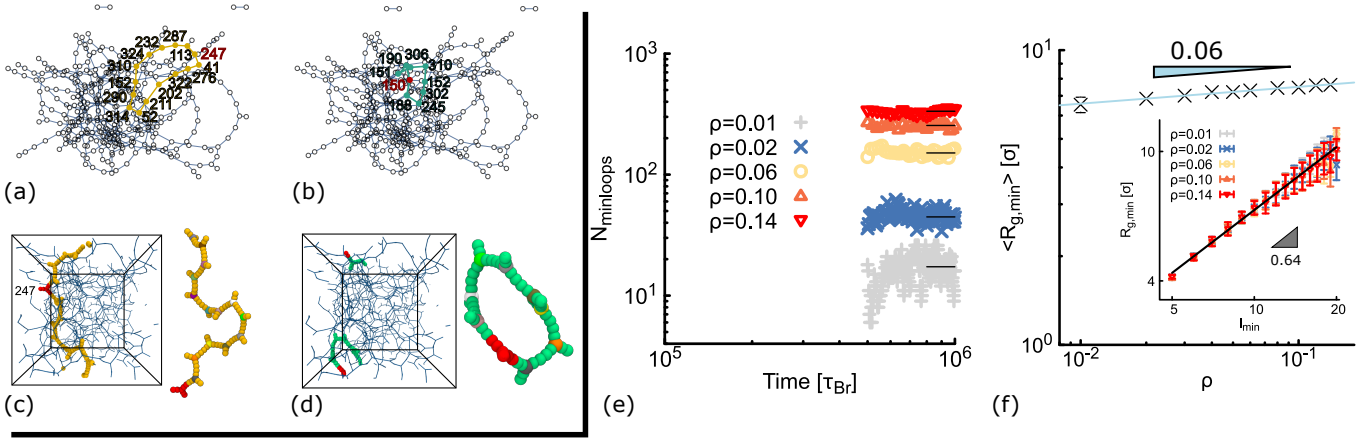

Figure S5. **Minimum loops analysis. (a)-(b)** Network diagram for the system with $\rho = 0.02$ and at $t = 10^6\tau_{Br}$ (same as the one in Fig. S2(a)). The minimum loop (highlighted in yellow (or green)) that passes through vertex 247 (or 150) (highlighted in red) is shown. The size of this minimum loop is $l_{min} = 15$ (or 9) nanostars. Labels depict the molecule IDs of nanostars. **(c)** Left panel shows the configuration from the simulation of the network diagram in (a). We use the minimum image criterion to reconstruct the correct path (right panel). To ease visualisation, the core beads of nanostars in the path are highlighted. **(d)** shows analogous results for the network diagram in (b). **(e)** Time evolution of the total number of minimum loops computed from simulations at times $t \geq 5 \times 10^5\tau_{Br}$ after turning on the attraction between patches. **(f)** Scaling of the average radius of gyration of the minimum loops as a function of ρ. Inset shows the plot of the radius of gyration (computed using Eq. S7) as a function of the size (l_{min}) for different concentrations of nanostars.

Fig. S5(f). The scaling exponents, $\langle R_{g,min}\rangle \sim \rho^{0.06}$ and $\langle l_{min}\rangle \sim \rho^{0.1}$, are consistent with our previous results from the analysis of the shortest path between branching points, $\langle R_{g,min}\rangle \sim \langle l_{min}\rangle^{0.6}$.

We also computed the average radius of gyration of the minimum loop as a function of l_{min}. Results for different concentrations are shown in the inset of Fig. S5(f), from which we obtain $\nu = 0.64$. These results confirm that $d_f = 1/\nu$ is independent of the concentration of nanostars, just as we found for the shortest path.

Linking number

The linking number between a pair of closed-oriented curves γ_i and γ_j can be computed through the numerical integration of the double integral:

$$\mathrm{Lk}(\gamma_i,\gamma_j) = \frac{1}{4\pi}\oint_{\gamma_i}\oint_{\gamma_j}\frac{(\mathbf{r}_j-\mathbf{r}_i)}{|\mathbf{r}_j-\mathbf{r}_i|^3}\cdot(\mathrm{d}\mathbf{r}_j\times\mathrm{d}\mathbf{r}_i), \qquad \text{(S8)}$$

where $\mathbf{r}_i$ and $\mathbf{r}_j$ are the vectors defining the position of all the points along the curves γ_i and γ_j, respectively. In our simulations, these curves are constructed from the set of beads in the minimum loops (not only core beads) identified from the analysis described in the previous section.

It is important to mention here some technical aspects that arise during the computation of the linking number in our system. (i) Since we reconstruct minimum loops (formed through the PBC) using the minimum image criterion, the linking between two rings could be overlooked. This happens when the initial beads in the two paths are not on the same side of the simulation box (see Fig. S6(a)). To account for the correct linking number, we perform the following analysis: After identifying the IDs of the set of beads forming two minimum loops and reconstructing them using the MIC, we compute their linking using Eq. S8. If Lk = 0, we reconstruct the second minimum loop starting from a different bead but keeping the order of particles in the loop (the *rotate function* in C++ is a good example of how to implement this). We continue with this calculation until either Lk $\neq$ 0 or we have performed all the possible rotations of the set of beads in the second minimum loop. (ii) We note that two minimum loops can share some vertices (see fig. S6(b)); this leads to numerical errors in the calculation of the linking number. Therefore, we use only pairs of disjoint rings which do not share vertices when computing Lk. (iii) The orientation of the minimum loops is randomly assigned due to the undirected nature of our graphs. Therefore, the value of Lk averaged over all the pairs of minimum loops is close to zero. However, to rationalize the elasticity observed in our simulations and measure how "entangled" the system is, we count the total number of times that two minimum loops are linked regardless of the sign of Lk:

$$\mathcal{L} = \sum_{i>j}^{N_{minloops}} |\mathrm{Lk}(\gamma_i,\gamma_j)|\,. \qquad \text{(S9)}$$

In Fig. S6(c), the time evolution of $\mathcal{L}(t)$ is shown. We observe that the total linking between minimum loops

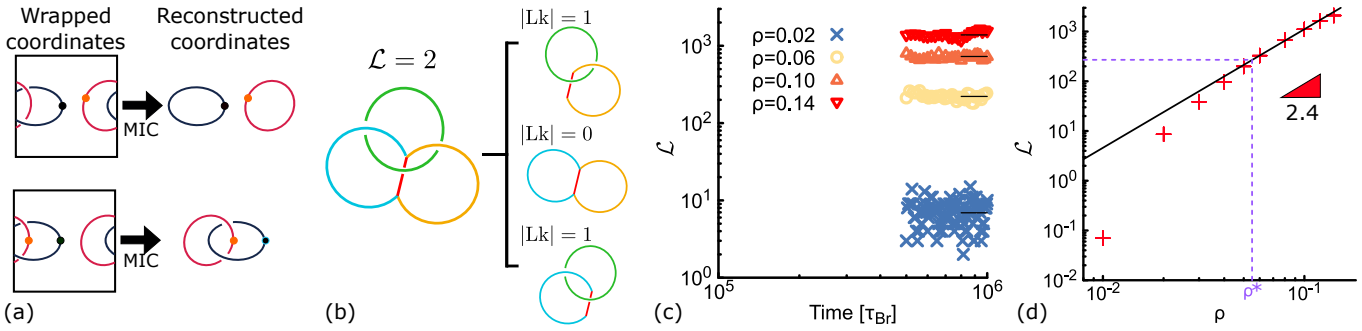

Figure S6. **Linking number analysis. (a)** Sketch of the reconstruction of two minimum loops using the minimum image criterion (MIC). The first particle in the set of beads in a minimum loop is represented by a dot (black and orange for the two different rings). The top panel shows the case where the reconstructed loops are not linked. In the bottom panel, a permutation that preserves the sequence of beads in the red minimum loop is applied. This is reflected in the change of the orange dot's position (with respect to the top panel) before applying the MIC. This time the reconstructed loops capture the correct linking between them. **(b)** Sketch of the linking number computed when two rings (the cyan and yellow) share vertices (region depicted in red) and interact with a third ring (in green). **(c)** Temporal evolution of the total linking number ($\mathcal{L}$), computed for different concentrations of DNAns. **(d)** Scaling of $\mathcal{L}$ with ρ.

reaches a plateau at long times. Fig. S6(d) shows the plot of the value of $\mathcal{L}$ at the plateau against concentration, from which the scaling $\mathcal{L} \propto \rho^{2.4}$ for ρ larger than the overlapping volume fraction, $\rho^* \sim 0.056$ (see below for computation), is found.

III. THE OVERLAPPING CONCENTRATION

The overlapping concentration (c^*) marks the point at which a solution is no longer dilute and polymer coils, or in this case nanostars, start to overlap. In experiments, c^* is obtained as:

$$c^* = \frac{M_w}{\frac{4}{3}\pi R^3 N_A}, \tag{S10}$$

where N_A is Avogadro's constant, M_w is the molecular weight of a single DNAns and R represents its radius of gyration [8]. Since a DNAns is made of 150 nucleotides, $M_w = 150 \times 650\text{Da}/2 = 48750 g/\text{mol}$. The value of the radius of gyration of a DNAns R is estimated by assuming that the double-stranded arms of a DNAns are rigid straight segments with a length of 20-26 base-pairs (depending if we count sticky-ends or not). Considering that the average height of a base-pair is $h = 0.34$ nm, we obtain $R = 6.8 - 8.84$ nm and therefore $c^* = 28.0 - 61.5$ mg/ml, or equivalently $c^* = 0.6 - 1.3$ mM.

In simulations, we expect that as we reach the overlapping concentration, the density of beads in the system ($7N/L^3$) is the same as the density of beads of a single DNAns ($7/V_{ns}$), where $V_{ns} = \frac{4}{3}\pi R^3$ is the volume occupied by a single DNAns with radius of gyration $R = 2.5\sigma$. Therefore $\frac{4}{3}\pi N^*(\frac{R}{L})^3 = 1$, from which we obtain the number of nanostars ($N^* = 978$) and the overlapping volume fraction $\rho^* = N^* V_{ns}/L^3 = 0.056$. Our simulations suggest that at ρ^* topological complex motifs like linking appear in the network, and therefore, ρ^* separates two regimes in the scaling of the mesh size (Fig. **2**(c)) and the average linking number per minimum loop (Fig. **4**(g)).

IV. DNA HYDROGELS PREPARATION

Oligonucleotide sequences (see Table S1) were acquired already purified with a standard desalting process from Integrated DNA Technologies (IDT, https://www.idtdna.com/pages). The oligo stocks are delivered in a dehydrated state. Therefore, before opening the tubes, we centrifuged them for 15-30s to guarantee that all dried DNA was pulled down to the bottom. Afterwards, the stocks were resuspended in Ultrapure Water to 1 mM, and we measured their concentrations employing a UV spectrophotometer (Thermo Scientific, NanoDrop Lite) after performing a series of dilutions in water at a ratio of 1:10, 1:100 and 1:1000. Once the concentration of each oligo was checked, we picked a volume from each stock for the three filaments to be equal in moles and mixed them into a single test tube. Then, we dehydrated the final solution at 60 °C for roughly 2h in a vacuum concentrator (Eppendorf, Concentrator *plus*) by leaving the tube opened with a sterilised filter on the top to avoid contamination. Once completely dried, the sample was dissolved in the Nanostar buffer (40 mM Tris, 40 mM sodium acetate, 1 mM EDTA (pH 8.0) and 150 or 500 mM NaCl depending on the experiment) [9] by alternating heating at 60°C and vortexing. The amount of buffer used depends on the final concentration desired for the experiments. Finally, we performed the annealing step by heating the sample to 90°C for 2 min in a well-isolated heat block and then cooling it slowly down until 25°C was reached in the block (over 4 h). Before per-

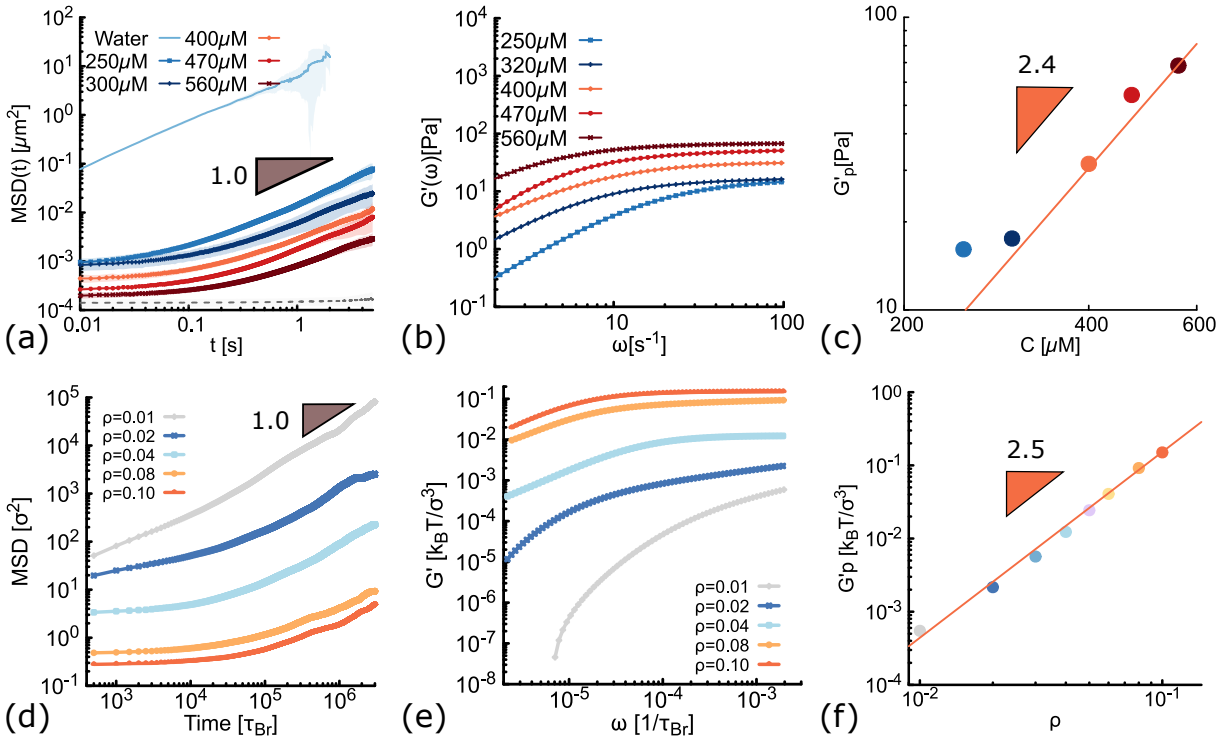

Figure S7. **Microrheology.** Top panels show experiment results, and the bottom panels are from simulations. **(a)** Examples of $MSD(t)$ obtained via PTM at different DNAns concentration. The grey dashed line shows the MSD of a bead immobilised on the glass surface. **(b)** Elastic modulus ($G'(\omega)$) as function of the frequency. **(c)** Elastic plateau obtained from the value of G' at 100 Hz. **(d)-(f)** show analogous results for the MR simulations.

forming any microrheology and confocal measurement, the concentration of the DNAns sample was checked using the same NanoDrop after 1:100 and 1:1000 dilution in water and following the calculations suggested in Ref. [9]. The DNA Nanostar solutions were then stored at 4°C.

V. MICRORHEOLOGY

In this section, we use particle tracking microrheology (PTM) to characterise the rheological properties of DNA hydrogels at different concentrations of DNA nanostars. In this technique, the stress relaxation moduli of a fluid are obtained from the mean squared displacement of spherical probes embedded in it. Here, we report the results obtained using PTM in both experiments and simulations.

Experimental protocol

Before starting the microrheology (MR) experiments, solutions at different concentrations of DNAns were prepared. Here we describe the preparation of a sample at a final concentration [DNAns]=500 μM; the generalisation of this protocol for different concentrations is straightforward. A total volume of 10 μL is used in all our microrheology experiments. We start by incubating an Eppendorf tube in a heat block set at 60°C and add: (i) 5μL of DNAns at 1 mM (49 μg/μL) pre-heated at 60°C for 2 minutes. (ii) 4.5μL of Nanostar Buffer (150mM NaCl, 1mM EDTA, 40mM Tris, 40mM Acetic Acid) to keep the salt concentration constant. (iii) 0.5 μL of 200 nm polystyrene beads (Sigma-Aldrich, d=1.05g/cm^3, concentration 10% solid), previously diluted in 1:500 in water. Once the beads are spiked in the solution, the samples are well mixed by pipetting 3-5 times via tips, which are also heated at 60°C to prevent quick cooling of the sample inside the tips and help the tracer particles' homogenisation into the self-assembling gel.

Samples are sandwiched between a glass slide and a cover slip to avoid drift and evaporation using a $\sim$ 100μm sticky spacer. The samples are left to equilibrate for a couple of minutes to reach 25°C in a stage-top temperature-controlled chamber (OKO Lab), which is placed on an inverted Nikon microscope and imaged with a 100x oil immersion objective in bright field mode. We restrict the field of view to 512x512 pixels and track 5-10 beads at 400 fps for 5 seconds. Recall that the typical bond lifetime between two sticky ends is roughly 0.1s at 25°C [9]. To extract the particles' trajectories, we use trackpy (`github.com/soft-matter/trackpy`) and com-

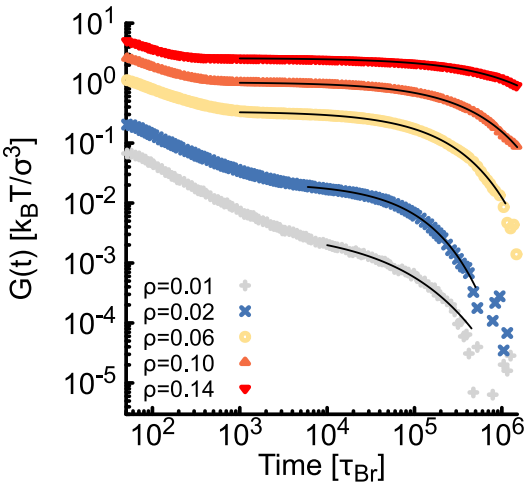

Figure S8. **Results from Green-Kubo simulations.** Autocorrelation of the stress-tensor obtained from equilibrium Green-Kubo simulations at different concentrations of nanostars. Points represent simulation results, and black lines are the fits of a stretch exponential function.

pute their mean squared displacement (MSD). To ensure good statistics, we tracked the same amount of beads in different positions of the sample. Figure S7(a) shows the results obtained.

To further characterise the viscoelastic properties of the system, we use the generalised Stokes-Einstein relation (GSER) to compute the complex stress modulus [10, 11]. Results of the elastic modulus as a function of the frequency are reported in Fig. S7(b), and the scaling of the high-frequency elastic plateau (G'_p) with the concentration in Fig. S7(c). Finally, experiments were repeated (from the preparation step) 2-3 times for each concentration. The results from all the experiments are reported in Fig. **1**(a) of the main text, in which we show that $G'_p \sim C^{2.5}$.

Simulations protocol

We simulate PTM experiments by introducing a 15σ diameter probe-particle (larger than the mesh size, see Fig. **2**(b) of the main text) in our simulation box. The excluded volume interaction of this particle is implemented via a purely-repulsive LJ potential, similar to the one in Eq. S1. The difference in particle size between the probe and nanostar beads can lead to a computationally inefficient integration of our system. Therefore, we use the *multi-style* of the neighbour command implemented in LAMMPS [5]. Each nanostar bead is subject to a translational drag μ that can be related to an inertial time scale $\tau_{in} = m/\mu$, i.e., the time over which the velocity decorrelates (directional information is lost). For a sphere, Stokes' law relates the drag to the viscosity of the solvent η: $\mu = 3\pi\eta d$, where d is the diameter of the sphere. Therefore the inertial time of a nanostar bead ($\tau_{in} = m/3\pi\eta\sigma = 1.0$) is set 15 times larger than that of the probe ($\tau_{in,p} = \tau_{in}/15 = 0.06$).

Once the probe particle is embedded into the solution of nanostars, we perform an equilibration run for $10^6\tau_{Br}$ time-steps, during which we prevent the attraction of nanostars ($\epsilon_m = 0$). Then, we reset the timestep to zero, turn on the attraction between nanostars and run the system for $5 \times 10^6\tau_{Br}$. The mean squared displacement of the probe-particle is reported in Fig. S7(d) for simulations at different concentrations of DNAns. As expected, the higher the concentration of nanostars, the slower the dynamics of the bead. Just as in experiments, we used the GSER to compute the complex stress modulus in Fig. S7(e). The elastic plateau G'_p in Fig. S7(f) is extracted as the value of G' at the largest frequency ($\omega \sim 2\times10^{-3}\tau_{Br}$). The scaling $G'_p \sim \rho^{2.5}$ is in agreement with the results found in experiments.

VI. GREEN-KUBO SIMULATIONS

The time-dependent mechanical response of a viscoelastic material in the limit of zero-deformation can be computed from the autocorrelation of the pressure tensor at equilibrium:

$$G(t) = \frac{L^3}{3k_BT}\sum_{\alpha\neq\beta} P_{\alpha\beta}(0)P_{\alpha\beta}(t), \qquad \text{(S11)}$$

where $P_{\alpha\beta}$ represents the out-off diagonal component (P_{xy}, P_{xz} and P_{yz}) of the stress tensor. The autocorrelation was computed using the multiple-tau correlator method described in reference [12] and implemented in LAMMPS with the *fix ave/correlate/long* command. This computation ensures that the systematic error of the multiple-tau correlator is always below the level of the statistical error of a typical simulation.

Results from long simulations ($5 \times 10^6\tau_{Br}$) at different concentration of nanostars are shown in Fig. S8. We observe that the autocorrelation function exhibits a power law decay at early times, followed by an intermediate plateau and ending with structural relaxation. This is a typical signature of a viscoelastic fluid [13]. The final decay of $G(t)$ is well fitted by a stretched exponential function, $G'_p\exp[-(t/\tau)^\beta]$ (solid lines in the figure), from which the elastic plateau G'_p reported in Fig **1** of the main text and the relaxation time (τ) are obtained.

VII. INTERPENETRATION FROM EXPERIMENTS

Our experiments aim to showcase the interpenetration in DNAns hydrogels by using two distinct types of 3-

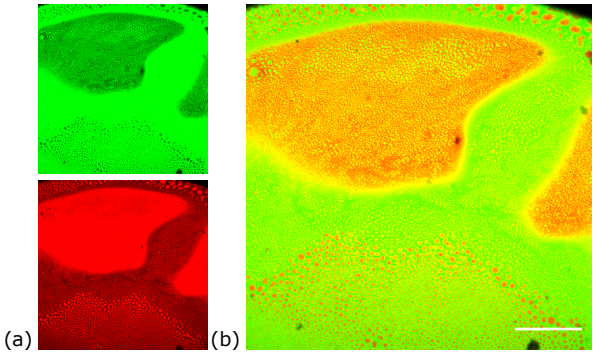

Figure S9. **Confocal image** of [DNS-A] and [DNS-B] at 500μM in 150mM NaCl. The image, taken after 240 min of sample sedimentation, shows the green and red channels split in **a** and then merged in **b**. The scale bar is 250 μm.

armed nanostar design: DNS-A and DNS-B. The core sequence of DNS-B is obtained by shuffling some base pairs of the DNS-A core so the two designs have the same composition and melting temperature but different sequences (refer to Table S2). The different core sequences are needed to avoid adhesion effects between the two types of nanostars due to the imperfect particle self-assembly and formation of unintended cross-linkers [14]. Still, we preserve their flexibility by keeping the unpaired adenosines at the core of the Y-shaped structure and preceding the overhangs. To ensure that only nanostars of the same type bind together when they are mixed, distinct sequences are designed for the sticky ends, each comprising 6 nucleotides, having equal self-binding strength: ΔG is -8.5 kcal/mol (at [NaCl]=150mM) and -9.3 kcal/mol (at [NaCl]=500mM) for DNS-A, while for DNS-B ΔG is -8.2 kcal/mol (at [NaCl]=150mM) and -9.0 kcal/mol (at [NaCl]=500mM). As expected, elevating the salt concentration makes the binding between nanostars energetically more favourable because of the reduced repulsion amongst negatively charged DNA bases. Consequently, it is shown an elevation of the melting temperature of the sticky ends with the salt concentration (see Table S3). These values are obtained using the analysis tool from NUPACK [15]. Knowing the T_{m2} was essential to determine the optimal conditions for our future experiments. To identify each design when mixed together, a specific dye molecule was introduced at a 9-nucleotide distance from the sticky end of one of three oligos: i6-FAMK for DNS-A and iCy3 for DNS-B. The oligos sequences were designed via NUPACK and purchased with the dye modifications from IDT.

The DNS-A and DNS-B stock solutions (at 1mM) are prepared as described in section IV but in two separate test tubes to prevent the formation of unintended secondary structures during the annealing step. In both cases, the fluorescently tagged and untagged oligomers are mixed at a molar ratio of 1:10 (or 1:20). From

DNS-A				
Segment I	FJC	Segment II	FJ	Sticky end
5′– CTGGATCCGCGGAAGCTTAA	AA	CGGAATTCGCATGGATCCCC	A	CGATCG –3′
5′– CTGGATCCGCGGAAGCTTAA	AA	CGGAATTCGCA/i6-FAMK/GGATCCCC	A	CGATCG –3′
5′– GGGGATCCATGCGAATTCCG	AA	CTGAATTCCCTGGGATCCCG	A	CGATCG –3′
5′– CGGGATCCCAGGGAATTCAG	AA	TTAAGCTTCCGCGGATCCAG	A	CGATCG –3′
DNS-B				
5′– GTCAATGCCCGCGGGCAATT	AA	GGGCATGGAATTCCGCATC	A	GCTAGC –3′
5′– GTCAATGCCCGCGGGCAATT	AA	GGGCATGGAATT/iCy3/CCGCATCC	A	GCTAGC –3′
5′– GGATGCGGAATTCCATGCCC	AA	CCCTTGGGAATTCGATCCCG	A	GCTAGC –3′
5′– CGGGATCGAATTCCCAAGGG	AA	AATTGCCCGCGGGCATTGAC	A	GCTAGC –3′

Table S2. Strand sequence used in the design of DNS-A and DNS-B with valence $f = 3$ for confocal experiments. For each nanostar type, the first and second row of the table shows the same oligo sequence, which differs only in the presence of the molecule dye inserted in Segment II. The oligo with the molecule dye encoded is used in the sample preparation in a ratio of 1:10 (or 1:20) concerning the unlabelled oligo.

Sequence	[NaCl]=150mM		[NaCl]=500mM	
	100μM	500μM	100μM	500μM
A:5′−CGATCG−3′	31°C	38°C	37°C	44°C
B:5′−GCTAGC−3′	30°C	37°C	36°C	43°C

Table S3. Melting temperatures of the sticky ends for DNS-**A** and DNS-**B** at [NaCl] equal to 150mM and 500mM by varying the DNA concentration from 100μM to 500μM; inside and outside the phase separation region respectively.

the nanostar stock solutions, we prepared samples at lower concentrations to investigate the contribution of interpenetration under three different conditions: inside (100μM), in proximity (250μM) and outside (400μM and 500μM) the phase separation region. Here, we report the sample preparation at final concentration [DNS-A]=250μM and [DNS-B]=250μM in a total volume of 10μL. We start by placing a test tube in a heat block set at 60°C and adding: (i) 5μL of Nanostar Buffer (at 150mM or 500mM NaCl, depending on the experiment). (ii) 2.5μL from DNS-A and DNS-B stocks both pre-heated at 60°C for 2 min. The solution is well mixed by pipetting 3-5 times via pre-heated tips; then it is heated at 60°C for another 2 min, and finally, 5μL of the sample is loaded on the slide.

The samples are visualised with a Zeiss LSM700 confocal microscope using a 20x (Numerical Aperture = 0.4) objective. As in microrheology experiments, the sample is left to equilibrate at 25°C for 5 minutes by placing a stage-top thermal chamber on the microscope stage. We captured z-stack images (512x512 pixels, with a zoom=0.5) over time with an interval of 30min for 10-17h. We used a scan time of 15.49s and a laser intensity equal to 2.4% (no bleaching effects were detected at this intensity value). During the image acquisition, the 488nm and the 555nm lasers scan the sample sequentially to excite FAMK(DNS-A, shown in green in the top left of Fig. S9(a)) and Cy3(DNS-B, shown in red in the bottom left of Fig. S9(a)), respectively. To visualise the final image, we assemble the two channels into one via Fiji [16].

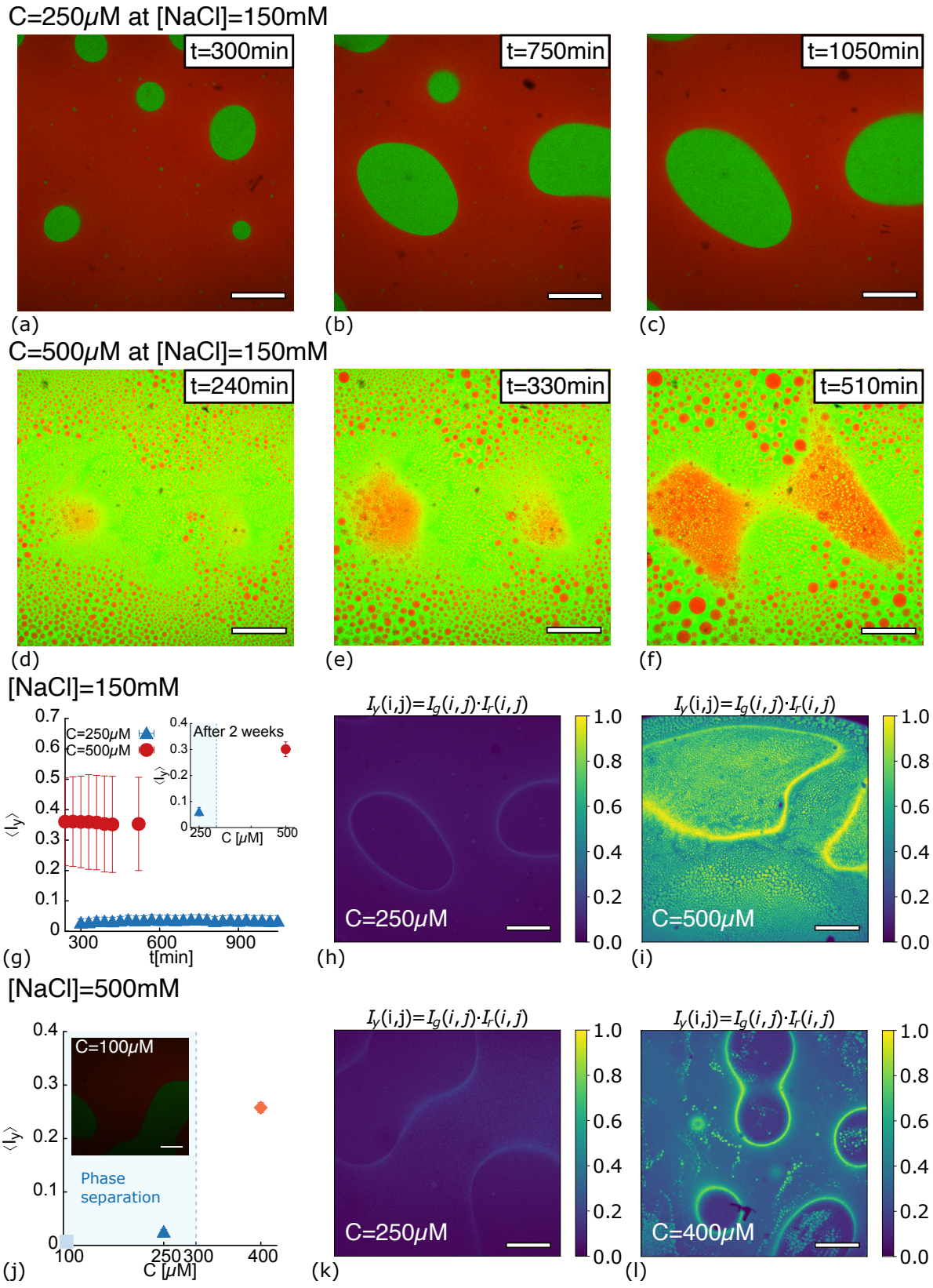

Figure S10. **Interpenetration analysis** Snapshots taken at different time points display the system's progression at DNA concentrations of 250uM **(a)-(c)** and 500uM **(d)-(f)** and at 150mM NaCl.**(g)** Intensity of the yellow component ($\langle I_y \rangle$) plotted as a function of time (in minutes) for C = 250 μM (blue triangle dots) and C= 500 μM (red circle dots) and at 150mM NaCl. The inset shows the average $\langle I_y \rangle$ of the samples from images taken after two weeks. Top panels show plots of the product matrix for 150mM NaCl and **(h)** C=250 μM and **(i)** C=500 μM. **(j)** Shows the value of $\langle I_y \rangle$ for samples at 500 mM NaCl and at C = 100, 250 and 400 μM. Inset shows a confocal image of a sample with C = 100 μM. Bottom panels show plots of the product matrix for 500mM NaCl and **(k)** C=250 μM and **(l)** C=400 μM. (Scale bars are 250 μm).

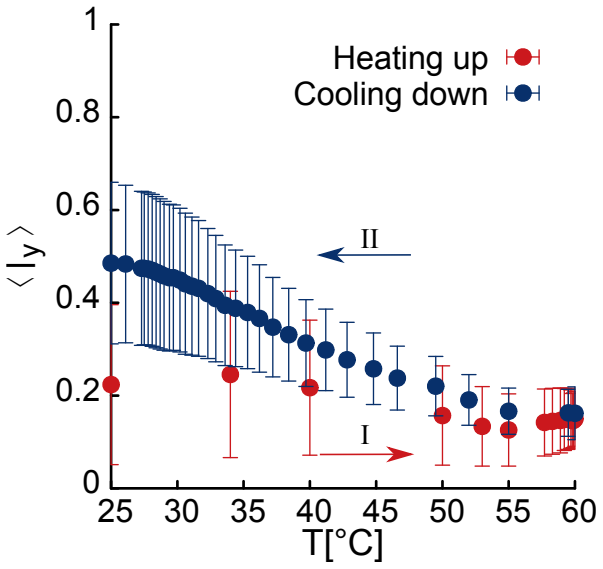

Figure S11. **Confocal results during and after temperature ramp.** This figure reports the behaviour of $\langle I_y \rangle$ in response to a temperature ramp performed with a temperature-controlled stage-top OKO Lab chamber. We place a sample of DNAns at 500 μM and 150 mM NaCl on the microscope at 25°C, heat the sample to 60°C and cool it back down to 25°C. We take images during the annealing and quenching and compute $\langle I_y \rangle$ as described above. One can appreciate that after the in situ annealing, the cooled sample appears to display a much stronger interpenetration.

As one can observe in Fig. S9(b), when [DNS-A]=500μM and [DNS-B]=500μM at [NaCl]=150mM, the image is partitioned into three dominant colours: green, red and yellow. Whilst it is evident the green component refers to the presence of DNS-A and the red one to DNS-B, the yellow part indicates the presence of regions/pixels populated by both the two types of nanostar. We interpret the abundance of yellow regions as signs of interpenetration. The yellow regions are seen mainly at the edges of red/green droplets where the two phases are in touch.

In Fig. S10, snapshots show the temporal evolution from confocal images of systems at [NaCl]=150mM. When C=250µM, panels (a)-(c) reveal there is no overlap between the green and red signals, indicating a complete demixing of the two components over time. On the other hand, the snapshots for C=500µM in panels (d)-(f) show that the mixed "yellow" regions persist and do not undergo demixing throughout the observation period. To better quantify the degree of interpenetration at different concentrations, we first split the images into two distinct channels and extract a 512x512 intensity matrix for the green (I_g) and one matrix for the red (I_r) channel. The elements of each matrix are integer numbers referring to the pixel values, which span from 0 to 255 (maximum value for an 8-bit image). Afterwards, we subtract the noise, obtained by taking an image with the same microscope settings on an empty slide, and set any negative value to zero. We then normalise the elements of both matrices by 255. Finally, to quantify the degree of mixing, we perform an element-wise multiplication consisting of multiplying each element of I_g with the corresponding element in I_r, as $I_g(ij) \cdot I_r(ij)$, to obtain a resulting matrix of dimension 512x512 (I_y). A first qualitative analysis was conducted by plotting a two-dimensional map of the I_g, I_r, and I_y matrices. For example, in Fig. S10(h-i), we plot the I_y matrix for different sample conditions: low values of $I_y(ij) \simeq 0$ (in dark violet) represent the presence of one of the 2 components, while high values of $I_y(ij) > 0$ (green to yellow) represent regions where the contribution of both channels is high. We highlight that values of the yellow product matrix are overall high at high concentrations of DNAns (500μM, see Fig. S10(i)) and overall very small in the case of low concentration of DNAns (250μM, see Fig. S10(h)). Increasing the salt concentration to [NaCl]=500mM produces similar results (Fig. S10(k-l)).

From the I_y matrix, we compute the average and the standard deviation across all entries to measure the overall extent of the yellow (interpenetration) signal across the image. In Fig. S10(g), the quantity of interest is denoted as $\langle I_y \rangle$, and it was computed for each image taken at a 30-minute interval. As one observes from the plot, the intensity of the yellow regions remains constant over time, displaying an average interpenetration of $\langle I_y \rangle \simeq 0$ for C=250µM and of $\langle I_y \rangle \simeq 0.4$ for C=500µM at [NaCl]=150mM. This stability of the "yellow" regions continues over weeks, as demonstrated in the inset of Fig. S10(g). The average intensity $\langle I_y \rangle$ at [NaCl]=500mM is reported in Fig. S10(j) for C=100, 250 and 400μM. We confirm that the green and red components do not overlap in the phase separation region, showing $\langle I_y \rangle \simeq 0$ for C=100μM and C= 250μM. In contrast, beyond the gel binodal at $C \leq 400\mu$M. Remarkably, we keep a greater interpenetration between the two components (Fig. S10(l))displaying an average of $\langle I_y \rangle \simeq 0.3$.

Temperature variations

To monitor the mixing/demixing behaviour of the binary DNAns system, we performed an in situ annealing/quenching on a sample by varying the temperature in the incubator chamber while recording images of the sample. Our first attempt involved DNS-A and DNS-B at a concentration of 500μM with 150mM NaCl. To start, we heated the sample to 60°C, which is above the melting temperature (T_{m2}) of the stick ends. This allows the molecules to diffuse freely in the solution. We then let the sample equilibrate for 15 minutes. Next, we adjusted the thermal chamber to 25°C to allow the nanostars to hybridise and form the network structure. The chamber temperature was tracked as the sample was

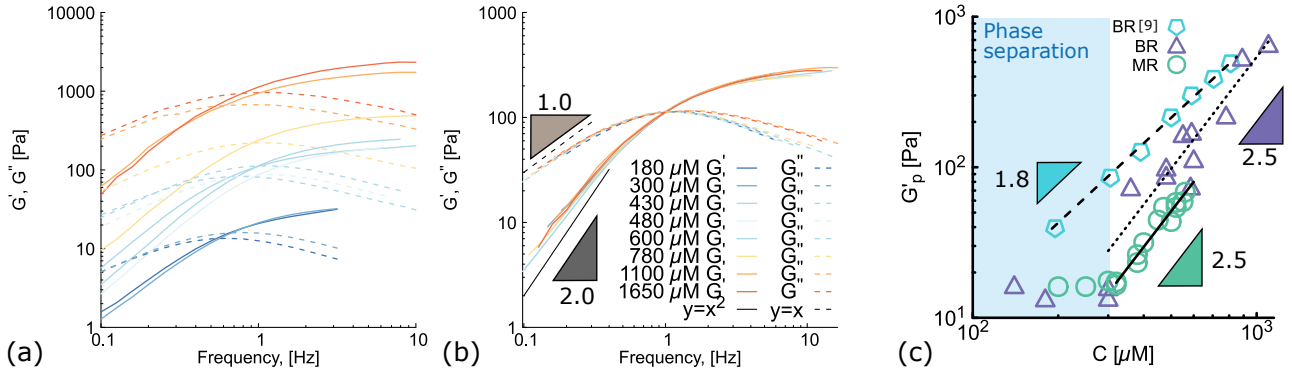

Figure S12. **Bulk rheology experiments. (a),(b)** show pre- and post-superposition frequency curves for a variety of DNAns concentrations (see inset legends). The lower concentration data is more truncated as inertial effects begin to dominate at the higher frequencies. In panel (a), as concentration increases, both G' and G" increase, except for DNAns that are within the phase separation region ($< 300\mu M$), which overlap with each other. In panel (b), we have applied Time-Temperature Superposition (TTS) to the curves (shifted relative to the 0.6mM curve), **(c)** Summary of results from BR (we report G_0) and MR experiments at different concentration of DNAns. The blue shadow area represents concentrations at which the system phase separates [4]. Previous BR experiments in reference [9] of gels made from DNAns with a slightly different design suggest a power law behaviour $G'_p \propto C^{1.8}$.

cooling for over 50 minutes. We captured an image every minute throughout the heating and cooling phases until the desired temperature was achieved. As we previously explained, we extracted the I_g, I_r, and I_y matrices from each picture and calculated the average ($\langle I_y \rangle$) and standard deviation of the product matrix. By plotting $\langle I_y \rangle$ against temperature (as shown in Fig. S11), we can effectively illustrate the effect of annealing/quenching on interpenetration. Our findings reveal that this in situ annealing/quenching protocol increases the extent of the interpenetration, eventually reaching 0.49 at 25°C. This final state is long-lived and displays an average interpenetration $\langle I_y \rangle \simeq 0.5$ for hours after the quenching protocol.

VIII. OSCILLATORY BULK RHEOLOGY

We employed bulk rheology (BR) to characterise the rheological properties of DNA hydrogels at different concentrations of nanostars. We utilise a stress-controlled Kinexus Pro rheometer by NETZSCH. In an identical manner to the samples made for MR, DNAns solutions at different concentrations were prepared (except that polystyrene beads were not added).

The DNAns solutions were pre-heated at 60°C for 2 minutes, then 100 μl was pipetted, using pre-heated tips, onto a flat 40 mm bottom plate. The top 40 mm plate was quickly closed to a 200 μm gap, the excess sample trimmed, and a solvent trap quickly fitted. The solvent trap uses mineral oil to create a temperature-stable seal and some wetted paper towel scraps within the chamber for rapid humidity equilibration. The sample is then re-heated to 60°C to re-anneal it before measurements are performed. We also attempted to replicate an oil seal as used by Conrad [9] but a mixing of the oil with the sample was observed post-measurements. This may be due to the temperature increase in this re-anneal step which lowers the surface tension of the oil.

For each concentration, an amplitude sweep was initially performed at a temperature of 20°C, frequency of 10 Hz, and a shear strain range of $\gamma = 0.1\% - 10\%$ to determine the linear viscoelastic region (LVR).

Frequency sweeps were subsequently performed at a shear strain of $\gamma = 0.5\%$ within the LVR. DNAns solutions behave like Maxwellian viscoelastic fluids, with low-frequency liquid behaviour ($G'' > G'$, with $G' \sim \omega^2$ and $G'' \sim \omega$) separated by a crossover frequency (ω_0), from high-frequency solid-like behaviour ($G' > G''$) and with a plateau modulus G'_p (see Fig. S12(a)).

After measurements were performed, DNAns were collected, and the concentration of DNA was re-measured. In all samples, the concentration of DNA post-measurement was found to have increased. This post-BR concentration was noted as the concentration of the sample.

From the frequency sweeps, it was possible to perform time-concentration superposition (TTS), Fig. S12(b), which shows that all the frequency curves overlap well above 300 μM. Below this point, they actually overlap before TTS is performed. Above 1 mM, a slight deviation in G" exists at high frequencies. Putting them in the Maxwell model's context is likely irrelevant as they are a viscous contribution on a time scale associated with solid behaviour.

In terms of determining how the plateau modulus G'_p scales with concentration TTS mean that this is equivalent to tracking how the crossover modulus G_0 (at which $G' = G''$) scales with concentration, and G_0 is signifi-

cantly easier to track being a well-defined point. This is displayed in Fig. **1** of the main text and in Fig. S12(c), where we also compare the results from BR, MR experiments performed here with the ones in reference [9].

* corresponding author, davide.michieletto@ed.ac.uk
† corresponding author, yair.fosado@ed.ac.uk

[1] J. N. Zadeh, C. D. Steenberg, J. S. Bois, B. R. Wolfe, M. B. Pierce, A. R. Khan, R. M. Dirks, and N. A. Pierce, Journal of Computational Chemistry **32**, 170 (2011).
[2] S. Biffi, R. Cerbino, G. Nava, F. Bomboi, F. Sciortino, and T. Bellini, Soft Matter **11**, 3132 (2015).
[3] N. R. Markham and M. Zuker, Nucleic Acids Research **33**, W577 (2005).
[4] N. Conrad, G. Chang, D. K. Fygenson, and O. A. Saleh, The Journal of Chemical Physics **157**, 234203 (2022).
[5] S. Plimpton, J. Comp. Phys. **117**, 1 (1995).
[6] M. Bantawa, B. Keshavarz, M. Geri, M. Bouzid, T. Divoux, G. H. McKinley, and E. Del Gado, Nature Physics (2023).
[7] W. R. Inc., "Mathematica, Version 13.3,".
[8] P. de Gennes, *Scaling concepts in polymer physics* (Cornell Univ. Pr., 1979).
[9] N. Conrad, T. Kennedy, D. K. Fygenson, and O. A. Saleh, Proceedings of the National Academy of Sciences **116**, 7238 (2019).
[10] T. G. Mason and D. A. Weitz, Physical Review Letters **74**, 1250 (1995).
[11] T. G. Mason, Rheologica Acta **39**, 371 (2000).
[12] J. Ramírez, S. K. Sukumaran, B. Vorselaars, and A. E. Likhtman, The Journal of Chemical Physics **133**, 154103 (2010).
[13] E. Flenner and G. Szamel, Physical review letters **114**, 025501 (2015).
[14] B.-j. Jeon, D. T. Nguyen, and O. A. Saleh, The Journal of Physical Chemistry B **124**, 8888 (2020).
[15] L. Hicks and J. Santalucia, Annual Review of Biophysics & Biomolecular Structure **33**, 415 (2004).
[16] J. Schindelin et al., Nature Methods **9**, 676 (2012).